Research Article Vol. 30, No. 26 / 19 Dec 2022 / Optics Express 47093

Optics EXPRESS

1 GHz electro-optical silicon-germanium modulator in the 5-9 µm wavelength range

THI HAO NHI NGUYEN,[1] NATNICHA KOOMPAI,[1] VICTOR TURPAUD,[1] MIGUEL MONTESINOS-BALLESTER,[1,3] JONATHAN PELTIER,[1] JACOPO FRIGERIO,[2] ANDREA BALLABIO,[2] RAFFAELE GIANI,[2] JEAN- RENÉ COUDEVYLLE,[1] CÉDRIC VILLEBASSE,[1] DAVID BOUVILLE,[1] CARLOS ALONSO-RAMOS,[1] LAURENT VIVIEN,[1] GIOVANNI ISELLA,[2] AND DELPHINE MARRIS-MORINI[1,*]

[1] *Université Paris-Saclay, CNRS, Centre de Nanosciences et de Nanotechnologies, 91120 Palaiseau, France*
[2] *L-NESS, Dipartimento di Fisica, Politecnico di Milano, Polo di Como, Via Anzani 42, 22100 Como, Italy*
[3] *Current affilliation: Institute for Quantum Electronics, ETH Zurich, Zurich, Switzerland*
[*] *delphine.morini@universite-paris-saclay.fr*

Abstract: Spectroscopy in the mid-infrared (mid-IR) wavelength range is a key technique to detect and identify chemical and biological substances. In this context, the development of integrated optics systems paves the way for the realization of compact and cost-effective sensing systems. Among the required devices, an integrated electro-optical modulator (EOM) is a key element for advanced sensing circuits exploiting dual comb spectroscopy. In this paper, we have experimentally demonstrated an integrated EOM operating in a wide wavelength range, i.e. from 5 to 9 µm at radio frequency (RF) as high as 1 GHz. The modulator exploits the variation of free carrier absorption in a Schottky diode embedded in a graded silicon germanium (SiGe) photonic waveguide.

© 2022 Optica Publishing Group under the terms of the Optica Open Access Publishing Agreement

1. Introduction

Mid-infrared spectroscopy is a universal tool to identify and detect small traces of hazardous and toxic substances due to the different vibrational and rotational resonances of molecules, leading to light absorption at specific wavelengths in the mid-IR. Numerous applications are thus foreseen in environmental detection, medical diagnosis, security and defenses [1–4]. Until now, most of the commercially available mid-IR equipment systems are bulky and expensive, meanwhile a variety of studies are focused to scale them down exploiting on-chip integration. Mid-IR integrated optical circuits is expected to be a key solution to develop compact, efficient, and portable sensing systems. Furthermore, silicon (Si) photonics is a solution of choice to take advantage of reliable and high-volume fabrication. Among the different integrated optical functions, a high-performance integrated EOM is expected to have a huge impact on spectroscopic systems. Indeed, dual comb spectroscopy has been demonstrated to be a unique tool enabling the scan of the optical spectrum with high frequency resolution, obviating step-by-step measurement in the frequency domain. It relies on optical frequency combs, which consists of regularly spaced, coherent lines in the frequency domain. In the mid-IR wavelength range, frequency combs have been successfully generated using different techniques including mode-locked lasers [5] frequency-modulated quantum cascade lasers [6], and optical nonlinear effects [7]. In parallel, electro-optic frequency comb based on optical modulators driven by a RF oscillator is also a promising alternative approach. With this technique, a frequency comb is generated around the wavelength of the laser source, with a line spacing given by the RF signal [8]. As a main advantage, the line spacing is thus fully tunable within the modulator bandwidth allowing a fine scanning of the optical spectrum. The electro-optical bandwidth of the modulator is then

#476164 https://doi.org/10.1364/OE.476164
Journal © 2022 Received 20 Sep 2022; revised 20 Nov 2022; accepted 22 Nov 2022; published 12 Dec 2022

Optics EXPRESS

a critical parameter to ensure a large tunability of the generated comb. Different studies have been reported in the literature towards high performance EOMs in the mid-IR. For instance, exploiting a GaAs/AlGaAs heterostructure, modulation up to 1.5 GHz has been obtained at 10 µm wavelength [9]. Alternatively, free-carrier plasma dispersion (FCPD) has been largely exploited in the near-infrared (NIR) and in the short-wave part of the mid-IR spectral range (below 4 µm wavelength) [10–13]. Recently, this effect has been extended in the long-wave part of the mid-IR. Indeed, a broadband integrated electro-absorption modulator has been demonstrated relying on a Schottky diode embedded in a SiGe waveguide. Absorption variation was obtained by modulation of the depleted region at the Schottky contact. Modulation has been demonstrated for wavelengths from 6.4 to 10.7 µm, operating at frequency up to 225 MHz [14,15]. The main challenges are now related with the improvement of the modulator performances in terms of efficiency and electro-optical bandwidth.

In this work, numerical simulations and experimental demonstrations are reported. First, the design and the optimization of coplanar waveguide electrodes were performed. Then, SiGe integrated EOM was fabricated and characterized. Experimental results show that the device operates from 5 to 9 µm wavelength, with an extinction ratio up to 1 dB. High speed operation is reported up to 1 GHz.

2. Results and discussion

2.1. Modulator design

The schematic cross-section of the integrated modulator is depicted in Fig. 1(a).

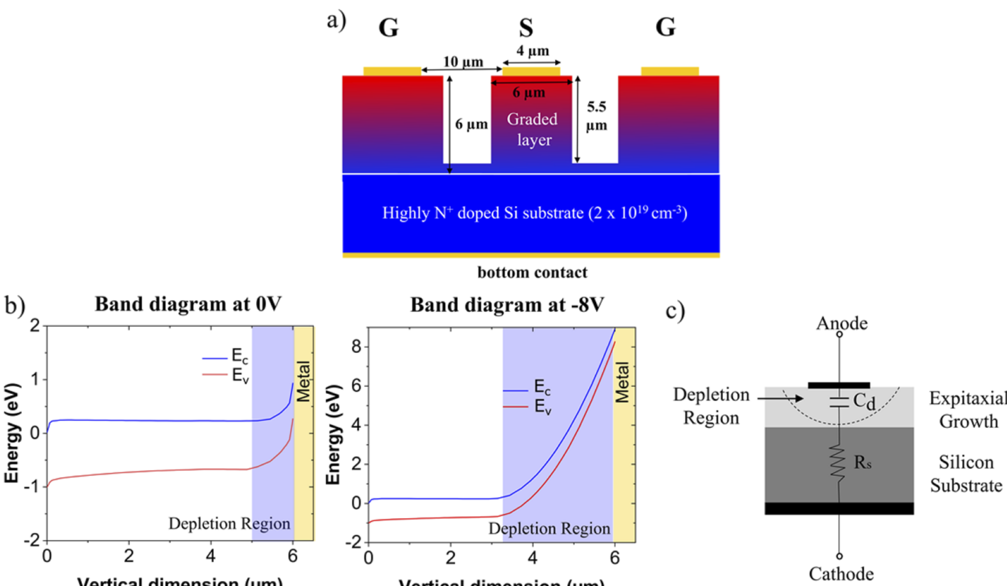

Fig. 1. Device design. a) Schematic cross-section view of the active region of the SiGe mid-IR integrated EOM. b) Simulated band diagram of the EOM structure with the valence band (red) and conduction band (blue) are plotted along the vertical direction of the SiGe epitaxial growth at different bias voltages of 0 V and -8 V. The change of the energy bandgap in the SiGe graded layer due to the evolution of the Ge concentration is clearly seen. The depleted region is highlighted in purple, its enlargement when reverse voltage increases is shown. c) Equivalent circuit of the device. The depletion region is located at the interface between the top contact metal and the semiconductor, thus the diode is formed vertically. The total series resistance R_s consists of contact and substrate resistances.

First, a 6-µm-thick graded SiGe layer is grown on a highly n-doped (Si) substrate with doping concentration of $2 \times 10^{19}\,\text{cm}^{-3}$. This Si layer is used as the bottom electrode with an electrical access from the backside of the sample. The graded SiGe layer is grown by linearly increasing the concentration of germanium (Ge) from 0 to 100%, inducing a linear increase of the refractive index in the waveguide. The graded epitaxial layer has a residual n-doped concentration estimated to be in the order of 10^{15}-$10^{16}\,\text{cm}^{-3}$. The waveguide width and etching depth are 6 µm and 5.5 µm, respectively. This waveguide geometry ensures a good mode confinement. At the top of the waveguide, a grounded coplanar waveguide (CPWG) electrodes based on a 300-nm-thick gold (Au) layer is deposited. The top contact on the lightly n-doped Ge layer is expected to feature a Schottky behaviour, while the bottom contact on highly n-doped Si is supposed to be an ohmic contact [15]. Figure 1(b) shows the calculated band diagram of the structure at bias voltages of 0 V and -8 V. It should be noted that the band gap energy in the SiGe layer varies along the vertical direction due to the Ge concentration gradient. When applying a negative voltage on the Signal electrical pad, the depth of the depleted region below the Schottky contact increases. The overlap between the optical mode and the free carriers region responsible for free carrier absorption decreases and so the absorption coefficient of the guided mode decreases, which corresponds to a modulation of the optical transmission of the guided mode. The transverse electric (TE) mode profiles are reported in Fig. 2 at different wavelengths (5.5, 7.8, and 9.0 µm).

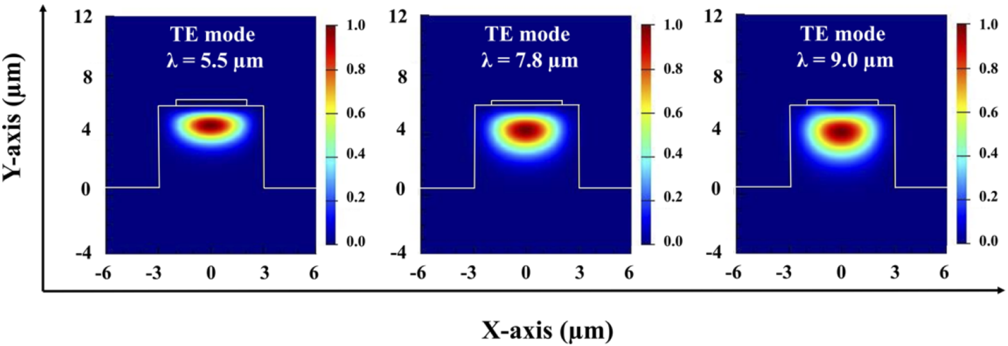

Fig. 2. Optical mode profiles in waveguide. TE optical modes at different wavelengths of 5.5, 7.8, and 9.0 µm. Scale bar: Normalized electric intensity.

To achieve high speed operation, a careful design of the electrical access and of the RF electrodes are performed, in order to (i) ensure an equivalent RC product compatible with high-speed operation, (ii) achieve impedance matching with the equipment used for the electro-optical characterization (50 ohms) avoiding high RF signal reflection and (iii) reduce the speed difference between electrical and optical signals propagating along the modulator. The use of grounded coplanar waveguide (CPWG) electrodes is investigated to that end. Numerical simulations are first performed to determine the impedance of the line and its transmission (S_{21}), considering the active region of the modulator integrated in the RF line. The equivalent electrical circuit of the Schottky diode, as shown in Fig. 1(c) is evaluated and added in the RF line modelling. The equivalent capacitance is extracted from capacitance-voltage characterizations, while the access resistance R_s is determined by current-voltage measurements, following the method in Ref. [16,17].

The main parameters for the CPWG electrode optimization are the width of the signal line path (W) and the gap between the metallic contacting pads (G). Considering fabrication tolerances, and knowing that the width of the photonic waveguide is 6 µm, the maximum value of W is fixed to 4 µm. First, the line impedance as a function of G is reported in Fig. 3(a), for a frequency of 5 GHz, and for 2 values of W (2 and 4 µm). It can be seen that W has a stronger influence than G

Optics EXPRESS

on the impedance parameter. Interestingly, 50 ohms matching can be obtained for W = 4 µm and G = 10 µm. S_{21} and line impedance are reported as a function of the frequency in Fig. 3(b) and Fig. 3(c), for G = 10 µm and two values of W (2 and 4 µm). It can be noticed that using W = 4 µm and G = 10 µm, low loss RF transmission is obtained up to 10 GHz, and the total characteristic impedance of the device is close to 50 ohms. Finally, the modulated optical power as a function of the frequency of the applied RF signal, normalized by the value at 10 MHz is evaluated (Fig. 3(d)). A distributed model, in which the device length is divided in 30 consecutive cells, is considered to take into account the propagation of the electrical and optical signals. The RF line parameters are W = 4 µm and G = 10 µm, and the equivalent electrical circuit of each portion of the modulator is considered within each cell. The bias applied on the diode capacitance is calculated all along the propagation which is used to determine the total modulated optical power. A 3 dB electro-optical bandwidth as high as 30 GHz is theoretically achievable.

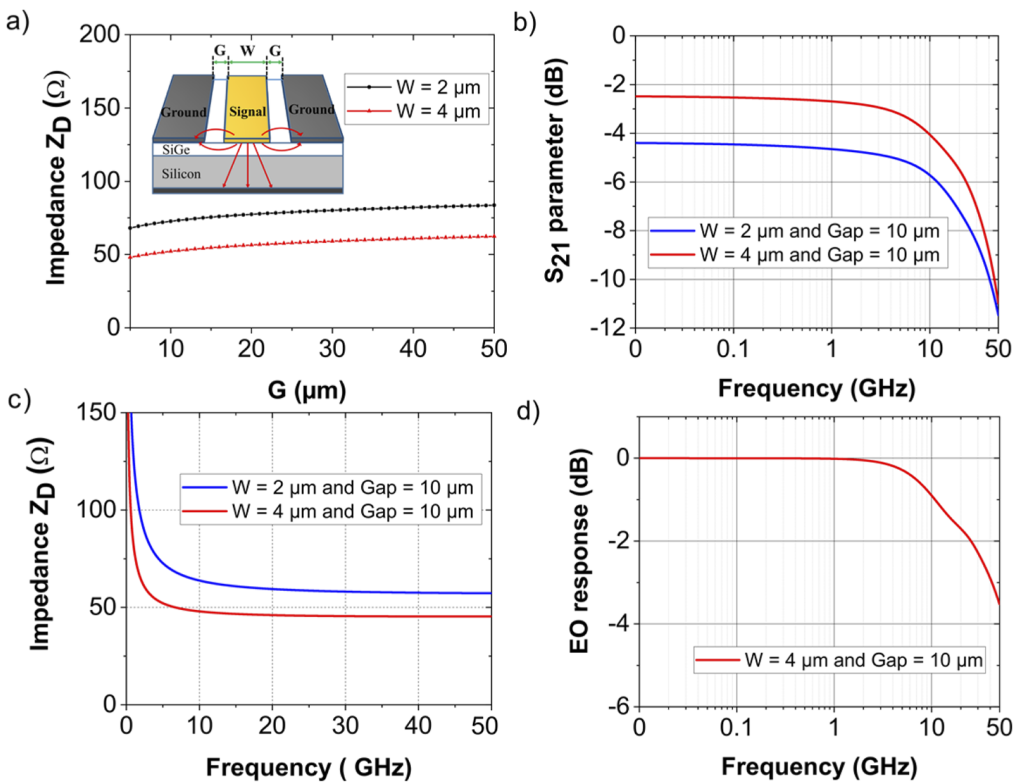

Fig. 3. Simulated electro-optical transmission responses in EOM. a) Dependence of the impedance on the gap between electrodes at frequency of 5 GHz. Inset, CPWG transmission line configuration with W-G dimension pairs. b-c) Electrical S-parameter S21 and impedance Z_D of the device as a function of RF frequency with different values of signal line widths of metallic contacting pads along 1.7-mm-long EOM, respectively. d) Electro-optical (EO) response with respect to RF frequency, normalized with the value at 10 MHz when W-G dimensions are optimized with 4 µm and 10 µm, respectively.

The schematic view of the waveguide-integrated device is reported in Fig. 4(a). The core of the integrated modulator is 500 µm long. The input light beam coming from an external laser is first butt-coupled to the photonic circuit via a 15-µm-wide input waveguide. Then, the waveguide width is narrowed down to 6 µm by a 200-µm-long adiabatic taper. To be able to contact the CPW electrodes with external RF probes, the waveguide must be enlarged, as can be

Optics EXPRESS

seen in Fig. 4. Multimode interferometer couplers (MMI) have been used to that end. Indeed, broadband 1 × 2 MMI have been reported before in the mid-IR range, using SiGe graded index photonics circuits [18]. From that preliminary work, 1 × 1 MMI has been designed as a solution to reach 50-μm-wide waveguide. Large bandwidth is expected from the simulation, with loss lower than 1.5 dB from 5 μm up to 9 μm wavelength. The total length of the modulator between both Ground-Signal-Ground (GSG) contact pads is 1.7 mm.

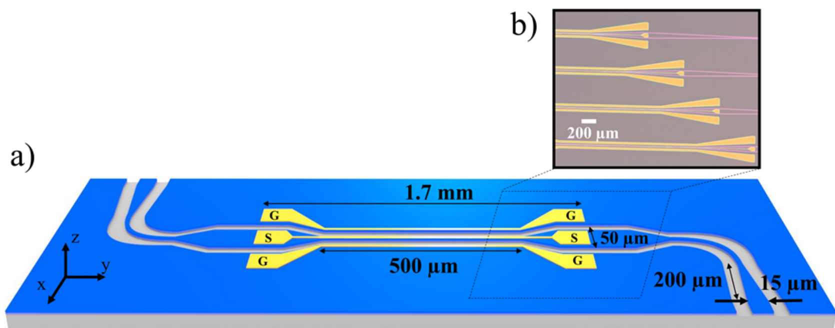

Fig. 4. Mid-IR integrated EOM circuit. a) Schematic view of the modulator. Both the optical and electrical paths can be seen. b) Microscope image of the fabricated device.

2.2. Fabrication and characterization of the modulator

The epitaxial growth of the SiGe graded layer on Si substrate is performed by low-energy plasma enhanced chemical vapour deposition (LEPECVD) [19]. Then, the modulator fabrication begins by a first lithography step to define the pattern of the top contacts. Metal is deposited (10-nm-thick titanium (Ti) followed by 300-nm-thick gold (Au)) followed by a lift off process. A second lithography step is carried out to pattern the photonic waveguides. ICP-RIE etching is then used to etch the 5.5-μm-deep waveguide. Finally, after a wafer backside polishing, the same metallic stack layers is deposited on the whole backside surface to form the bottom ohmic contact. An optical microscope picture of the final fabricated device can be seen in Fig. 4(b).

Current-voltage (I-V) characterization of the modulator is reported in Fig. 5(a). A good rectifying behavior is obtained, which confirms that a depletion region is formed at the top of the waveguide. From this measurement, a Schottky barrier of 0.58 eV can be extracted, with a diode ideality factor of 1.44, which is consistent with the similar device reported in Ref. [15]. On the other hand, the I-V characterization in the injection (forward) regime can be used to estimate the series resistance of the device, which is approximately 2.5 Ω.

Capacitance-voltage (C-V) characterization is used to characterize the depletion region below the top contact. The C-V measurement has been performed on different specific square-shaped mesa fabricated on the same chip. The variation of the diode capacitance per unit area with respect to the voltage is reported in Fig. 5(b). As expected, the capacitance decreases with the increase of the reverse voltage demonstrating the enlargement of the depleted region.

The EOM is then characterized, and different figure of merits are deduced. First, the mode loss due to the influence of the top metal is experimentally estimated comparing the optical transmission of two devices which differs only for the presence or not of the top metallic layer. Interestingly a good agreement between this measurement and the results from numerical simulation are obtained (see Fig. S1). Then the waveguide propagation loss has been determined using the cut-back method. Finally, the total insertion loss (IL) of the 1.7-mm-long modulator is evaluated to be about 2.5 dB, 4.5 dB and 10.5 dB for wavelengths of 5.5 μm, 7.8 μm, and 9 μm, respectively.

Optics EXPRESS

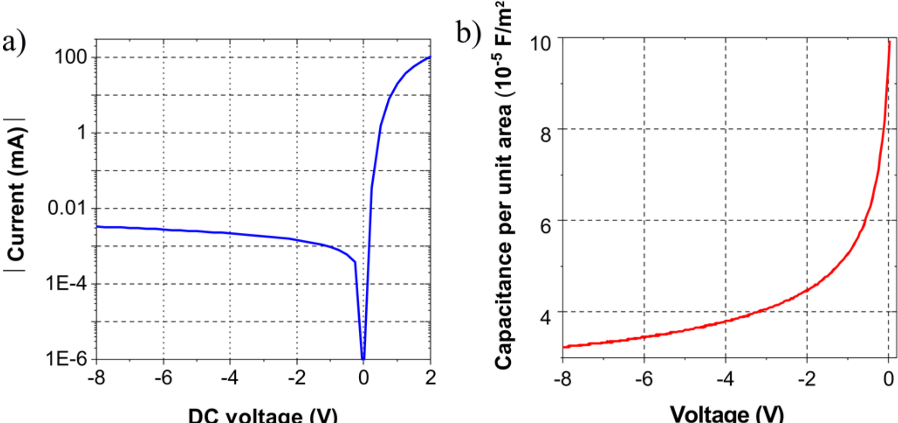

Fig. 5. Electrical characterization. A) Dark I-V characterization of the device. B) Variation of the diode capacitance as a function of the applied voltage, extracted from square mesa fabricated on the same sample.

The modulation efficiency is then characterized in the depletion regime. The relative optical transmission (normalized with the optical transmission at zero bias) is reported in Fig. 6 as a function of the reverse bias voltage and for wavelengths from 5.5 to 9 µm. It can be noticed that the optical transmission increases when the amplitude of the reverse voltage increases. This behavior is explained by the expansion of the space charge region, thus the overlap between the optical mode and the free carrier region decreases leading to a decrease of the total absorption coefficient of the optical mode. It can be noticed that the modulation efficiency increases for higher wavelengths, which is in good agreement with the FCPD effect [20]. An extinction ratio higher than 1 dB is obtained at the wavelength of 9 µm with -8 V applied to the device.

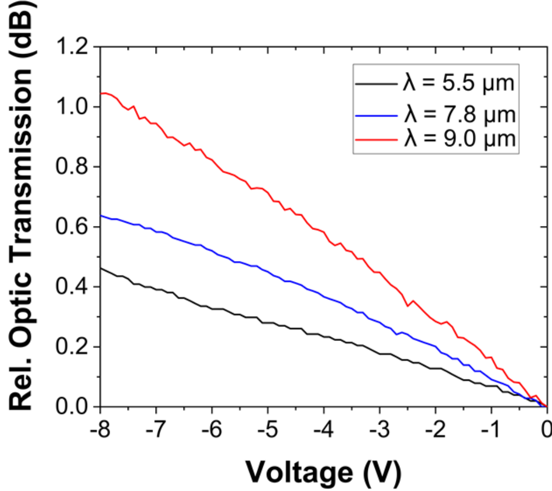

Fig. 6. EOM static characteristics. Relative optical transmission as a function of the reverse bias voltages for different wavelengths.

Finally, high-speed characterizations have also been performed. An RF electrical signal is added to the reverse DC bias using a bias tee. The electrical signal is applied to the modulator by

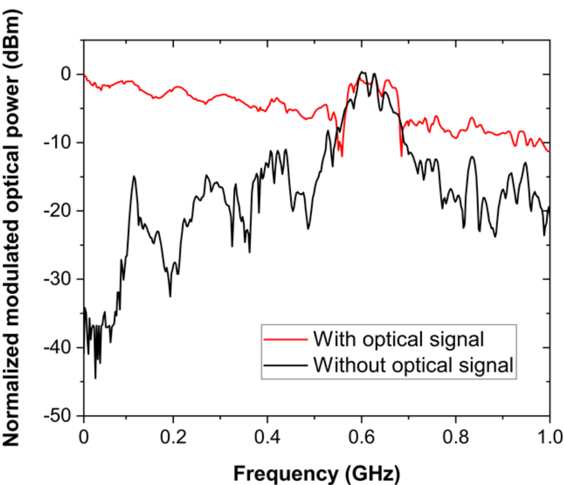

Fig. 7. EOM frequency characterization. Variation of the modulated optical power with the applied RF frequency (red curve) in depletion region with 5 Vpp and -4 V bias applied on the device. The measurement is reported at 7.8 μm wavelength and is normalized with the response at 10 MHz. The amplitude of the detected signal due to the noise level of the detection scheme is also reported (black curve).

the external probes. The light coming out of the device is sent to a fast mid-IR detector and an electrical spectrum analyzer is used to acquire the corresponding beat notes. The peak amplitudes are recorded to characterize the evolution of the modulated optical power as a function of the applied RF frequency (Fig. 7). The electrical signal applied on the modulator is composed of a 5 V peak to peak (5 V_{pp}) modulated RF signal added to the -4 V bias DC voltage, in order to stay within the depletion regime. The modulated optical power as a function of the RF signal frequency is normalized with the response at 10 MHz. The measured signal coming from the

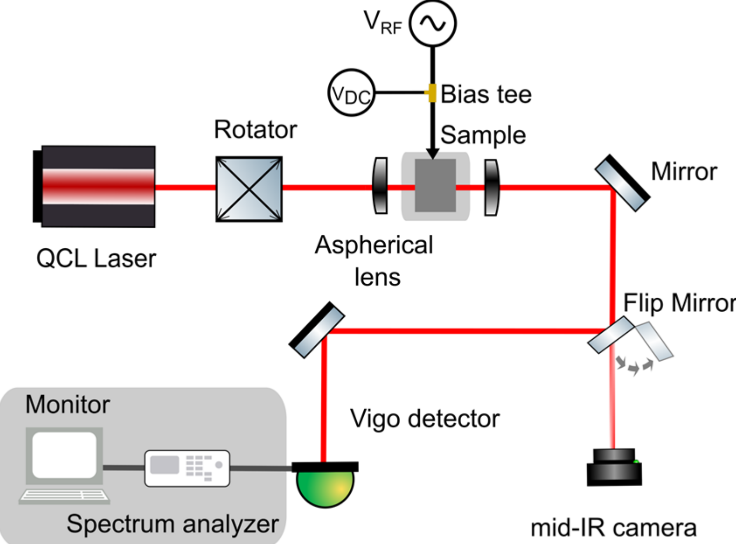

Fig. 8. Experimental dynamic EOM characterization.

EOM is also compared with the noise level measured in the same configuration, by turning off the input laser. As it can be seen in Fig. 7, measurements between 500 MHz and 700 MHz are limited by the high noise level of the detector at this frequency range. Nevertheless, a slow decrease of the modulated optical signal is observed as a function of the RF frequency. The time constant of the photodetector itself (specified to be below 25 ns) is expected to explain, at least partially, this evolution. However, optical modulation is measured up to 1 GHz where a signal to noise ratio larger than 10 dB is still obtained. No sharp drop is seen even at this frequency which indicates that the modulator can probably operate at higher frequencies. Unfortunately, due to the limitation of the experimental set-up in terms of noise and cut-off frequency of the detector, the measurements at higher frequencies are not achievable.

3. Discussion

While this work reports the first integrated and wideband mid-IR electro-optical modulator operating up to 1 GHz frequency, different routes of improvement can be discussed.

First, the reported high-speed measurements are for the moment limited by the cut-off frequency of the detector, and the contribution of the detector bandwidth and cables have not been removed from the measurement. Further investigation of this device at higher frequencies will then require optimizing the experimental set-up.

In a second step, improving the modulator performances in terms of losses and extinction ratio can be considered. Different routes can be pursued, by optimizing either the dopant distribution in the waveguide or even to optimize the SiGe gradient profile to engineer the mode profile in the diode.

4. Conclusion

In conclusion, this work is a step forward the realization of high performance integrated electro-optical devices operating in long-wavelength range in the mid-IR range. A specific care has been paid on the modelling and optimization of coplanar waveguide electrodes to drive a SiGe EOM based on the FCPD effect. Efficient modulation has been experimentally demonstrated from 5.5 to 9 µm wavelength. Furthermore, high speed operation has been investigated and 1 GHz electro- optical modulation is experimentally demonstrated. This measurement was done at a fixed wavelength of 7.8 µm, but it can be noticed that the device speed does not depend on the input wavelength. Such results pave the way towards the use of EOM in fully integrated systems in the mid-IR spectral ranges. Moreover, the realization of high-speed EOMs also paves the way for free-space communications, especially for satellite communications within the atmospheric transparent windows (3-5 µm and 8-14 µm wavelengths).

5. Methods

5.1. Static and dynamic EOM setup

Static EOM setup: A mid-IR quantum-cascaded laser (MIRCAT, Daylight solution) with a pulse rate of 100 kHz and a duty cycle of 5% is used to cover a wide spectral range from 5.2 µm up to 11 µm. The light emitted from the QCL is butt-coupled to the photonic chip by ZnSe aspherical lens. 5 dB/ facet coupling loss is expected from this coupling scheme. The light at the output of the device is collected and detected by an MCT detector (DSS-MCT-020, Horiba) which is connected with lock-in detection system to amplify the signal. In order to provide the DC voltage to the modulator, a source-meter equipment (Keithley 2400) is used and connected with RF probes.

Dynamic EOM setup: High-speed measurements are performed using a continuous-wave QCL at the wavelength of 7.8 µm (MIRcat, Daylight Solutions), depicted in Fig. 8. The output beam light is detected by a MCT detector (PVI-4TE-10.6, Vigo System). After being pre-amplified (FIP

series, Vigo System), the signal is detected by a signal analyzer equipment (MS2830A, Anritsu). The DC and AC signals are applied to the RF probes through a bias tee with a source-meter equipment (Keithley 2400) and signal generator (MG3694C, Anritsu), respectively.

5.2. Simulation

Numerical simulations of the optical profile are performed using finite different eigenmode (FDE) in Lumerical Software (2021). The equivalent transmission line of optical modulator is simulated by automation software system Advanced Design System (ADS), thus S-parameter S_{21}, impedance Z_D and EO response are extracted from the simulations.

Funding. Renatech; Fondazione Cariplo (2020–4427, 2020–4427 (Milestone)); Agence Nationale de la Recherche (ANR-19-CE24-0002-01).

Acknowledgments. The fabrication of the device was partially performed at the Platform de Micro-NanoTechnologie/ C2N, which is partially funded by the "Conseil Général de l'Essonne". This work was partly supported by the French RENATECH network. L-NESS laboratory is also acknowledged for SiGe epitaxial growth.

Disclosures. The authors declare no conflicts of interest.

Data availability. Data underlying the results presented in this paper may be obtained from the authors upon reasonable request.

Supplemental document. See Supplement 1 for supporting content.

References

1. G. Z. Mashanovich, M. Nedeljkovic, J. Soler-Penades, Z. Qu, W. Cao, A. Osman, Y. Wu, C. J. Stirling, Y. Qi, Y. X. Cheng, L. Reid, C. G. Littlejohns, J. Kang, Z. Zhao, M. Takenaka, T. Li, Z. Zhou, F. Y. Gardes, D. J. Thomson, and G. T. Reed, "Group IV mid-infrared photonics," Opt. Mater. Express **8**(8), 2276–2286 (2018).
2. H. Lin, Z. Luo, T. Gu, L. C. Kimerling, K. Wada, A. Agarwal, and J. Hu, "Mid-infrared integrated photonics on silicon: a perspective," Nanophotonics **7**(2), 393–420 (2017).
3. D. Marris-Morini, V. Vakarin, J. M. Ramírez, Q. Liu, A. Ballabio, J. Frigerio, M. Montesinos Ballester, C. Alonso-Ramos, L. R. Xavier, S. Serna, D. Benedikovic, D. Chrastina, L. Vivien, and G. Isella, "Germanium-based integrated photonics from near- to mid-infrared applications," Nanophotonics **7**(11), 1781–1793 (2018).
4. T. Hu, B. Dong, X. Luo, T.-Y. Liow, J. Song, C. Lee, and G.-Q. Lo, "Silicon photonic platforms for mid-infrared applications," Photonics Res. **5**(5), 417–430 (2017).
5. A. Schliesser, N. Picque, and T. Haensch, "Mid-infrared frequency combs," Nat. Photonics **6**(7), 440–449 (2012).
6. J. Faist, G. Villares, G. Scalari, M. Rosch, C. Bonzon, A. Hugi, and M. Beck, "Quantum Cascade Laser Frequency Combs," Nanophotonics **5**(2), 272–291 (2016).
7. M. Yu, Y. Okawachi, A. Griffith, N. Picqué, M. Lipson, and A. Gaeta, "Silicon-chip-based mid-infrared dual-comb spectroscopy," Nat. Commun. **9**(1), 1869 (2018).
8. V. Torres-Company and A. M. Weiner, "Optical frequency comb technology for ultra-broadband radio-frequency photonics," Laser Photonics Rev. **8**(3), 368–393 (2014).
9. S. Pirotta, N. Tran, A. Jollivet, G. Biasiol, P. Crozat, J.-M. Manceau, A. Bousseksou, and R. Colombelli, "Fast amplitude modulation up to 1.5 GHz of mid-IR free-space beams at room-temperature," Nat. Commun. **12**(1), 799 (2021).
10. M. A. Van Camp, S. Assefa, D. M. Gill, T. Barwicz, S. M. Shank, P. M. Rice, T. Topuria, and W. M. J. Green, "Demonstration of electrooptic modulation at 2165 nm using a silicon Mach-Zehnder interferometer," Opt. Express **20**(27), 28009–28016 (2012).
11. D. J. Thomson, L. L. Shen, J. J. Ackert, E. Huante-Ceron, A. P. Knights, M. S. Nedeljkovic, A. C. Peacock, and G. Z. Mashanovich, "Optical detection and modulation at 2µm-2.5 µm in silicon," Opt. Express **22**(9), 10825–10830 (2014).
12. J. Kang, M. Takenaka, and S. Takagi, "Novel Ge waveguide platform on Ge-on-insulator wafer for mid-infrared photonic integrated circuits," Opt. Express **24**(11), 11855–11864 (2016).
13. D. Perez-Galacho, D. Marris-Morini, R. Stoffer, E. Cassan, C. Baudot, T. Korthorst, F. Boeuf, and L. Vivien, "Simplified modeling and optimization of silicon modulators based on free-carrier plasma dispersion effect," Opt. Express **24**(23), 26332–26337 (2016).
14. J. M. Ramirez, Q. Liu, V. Vakarin, J. Frigerio, A. Ballabio, X. Le Roux, D. Bouville, L. Vivien, G. Isella, and D. Marris-Morini, "Graded SiGe waveguides with broadband low-loss propagation in the mid infrared," Opt. Express **26**(2), 870–877 (2018).
15. M. Montesinos-Ballester, L. Deniel, N. Koompai, T. H. N. Nguyen, J. Frigerio, A. Ballabio, V. Falcone, X. Le Roux, C. Alonso-Ramos, L. Vivien, A. Bousseksou, G. Isella, and D. Marris-Morini, "Mid-infrared Integrated Electro-optic Modulator Operating up to 225 MHz between 6.4 and 10.7 µm Wavelength," ACS Photonics **9**(1), 249–255 (2022).
16. S.M. Sze, *Physics of Semiconductor Devices* (Wiley-Intersicence, 1969).

Optics EXPRESS

17. C. R. Crowell, "Richardson constant and tunneling effective mass for thermionic and thermionic-field emission in Schottky barrier diodes," Solid. State. Electron **12**(1), 55–59 (1969).
18. V. Vakarin, J. Ramirez, J. Frigerio, A. Ballabio, X. Le Roux, Q. Liu, D. Bouville, L. Vivien, G. Isella, and D. Marris-Morini, "Ultra-wideband Ge-rich silicon germanium integrated Mach-Zehnder interferometer for mid-infrared spectroscopy," Opt. Lett. **42**(17), 3482–3485 (2017).
19. C. Rosenblad, H. R. Deller, A. Dommann, T. Meyer, P. Schroeter, and H. von Kanel, "Silicon epitaxy by low-energy plasma enhanced chemical vapor deposition," J. Vac. Sci. Technol., A **16**(5), 2785–2790 (1998).
20. M. Nedeljkovic, R. Soref, and G. Z. Mashanovich, "Predictions of Free-Carrier Electroabsorption and Electrorefraction in Germanium," IEEE Photonics J. **7**(3), 1–14 (2015).

131.175.147.2 {ts '2023-01-10 04:57:38'}